



Extraction of Hydroxyapatite from Fish Bones and Its Application in Nickel Adsorption

Seyed Mohammad Hossein Dabiri¹ · Amir Ardalan Rezaie² · Mehrnaz Moghimi³ · Hamidreza Rezaie⁴

© Springer Science+Business Media, LLC, part of Springer Nature 2018

Abstract

Precious materials obtained from biowaste have risen the attentions toward extracting and using these materials in various applications to address both economic and environmental demands. In the present study, we focused on the extraction of hydroxyapatite (HA) from fish bones through the thermal calcination method. The primary tests were carried out to characterize the fish bone-derived materials in terms of chemical composition, morphology, and viability. Therefore, series of characterizing tests including Fourier transform infrared spectroscopy (FT-IR), X-ray diffraction (XRD), and inductively coupled plasma (ICP) were carried out. Also, secondary electron microscopy equipped with energy-dispersive spectroscopy (EDS) was performed to determine morphology and elemental analysis of the obtained powder. Furthermore, the cell viability of fish bone-derived hydroxyapatite (FHA) along with its cell differentiation capability was evaluated by performing MTT and ALP assays and the results were compared with those of the commercial type of hydroxyapatite (CHA). The secondary phase of the current study relates to the capability of FHA and CHA on adsorbing nickel, as a model heavy metal, from aqueous solutions by performing bath adsorption experiments and considering initial concentration of nickel, adsorbent dosage, and contact time as the variables. In order to investigate kinetic model and adsorption mechanism, first-order, pseudo-second-order, and intraparticle diffusion kinetic models were used. Also, the equilibrium data were analyzed using Langmuir, Freundlich, and DKR adsorption isotherm models. The XRD and FT-IR results confirmed the successful extraction of HA from fish bones. Besides, ICP and EDS results revealed that the Ca/P ratio of FHA was higher than that of stoichiometric ratio (1.67). In addition, the MTT and ALP results indicated that FHA seemed to be a viable material for cell proliferation and differentiation. Besides, the adsorption outcomes indicated that FHA was sufficiently capable of adsorbing nickel. It was observed that the adsorption data were fitted well with pseudo-second-order and Langmuir isotherm models with maximum adsorption capacities of 50.25 and 48.78 mg g⁻¹ on FHA and CHA, respectively.

Keywords Hydroxyapatite · Thermal calcination · Physicochemical characterizations · Adsorption isotherm · Kinetic study

Highlights

- Fish bone-derived hydroxyapatite (FHA) powder was obtained via thermal calcination method.
- The extraction method is easy, economical, and favorable for environmental concerns.
- The FHA powder showed proper cell viability compared to commercial hydroxyapatite (CHA).
- Both FHA and CHA powders expressed almost similar performance in the adsorption of nickel.
- The experimental results were in accordance with pseudo-second-order equation.
- The nickel adsorption parameters were well fitted with Langmuir equations.

✉ Seyed Mohammad Hossein Dabiri
mohammadhossein.dabiri@gmail.com

¹ Department of Informatics, Bioengineering, Robotics, and System Engineering, University of Genoa, Genoa, Italy

² Department of Materials Science and Engineering, University of California, Riverside, Riverside, CA, USA

³ Department of Natural Resources (Fisheries Division), Isfahan University of Technology, Isfahan, Iran

⁴ Department of Materials Science and Engineering, Iran University of Science and Technology, Tehran, Iran

1 Introduction

According to the statistics published by the Food and Agricultural Organization (FAO), globally more than 150 million tons of fish, crustaceans, molluscs, and other aquatic animals were produced in 2011. They also estimated that about 85%, 132 million tons, of total fishery production was used for human consumption [1]. About 20–30 million tons of fish wastes are thrown away in the world each year [2]. Despite that these waste materials are potential sources of valuable products including high biological proteins, vitamins, antioxidants, enzymes, collagens, and minerals [3], the majority of these materials are used for animal meal production. Hence, in order to reduce pollution and environmental effects of fish waste materials, high added value by-products and extraction of valuable components from these raw materials would be recommendable.

It was found that nearly 30–40% of total fish production are wasted. In addition, the fish scales are the major solid by-products of fish product industries [4]. Although fish scale used to be considered as an inconsequential waste material, it is known as a cheap source of precious components such as collagen and calcium phosphates [5–9]. Hydroxyapatite (HA), $\text{Ca}_{10}(\text{PO}_4)_6(\text{OH})_2$, the major component of human bones, is the most important calcium phosphate which has outstanding biocompatibility, osteoconductivity, and osteoinductivity characteristics. These excellent characteristics of hydroxyapatite were the driving force to use hydroxyapatite in the medical applications including implant and/or coating materials [10–13].

Hydroxyapatite can be synthesized via different methods like hydrothermal [14], solid state reaction [15], chemical precipitation [16], radio frequency thermal plasma [17], and polymer assisted [18]. The hydroxyapatite obtained from animal bones exhibits some advantages over the synthetic ones such as chemical composition and structure close to those of the human bone, lower cost process, availability in an unlimited supply, and improved biological response [19–23]. Bovine bones [24], bones and teeth of pigs [25], and fish bones [26] are some example of natural sources of HA.

Several researches have been focused on the extraction of HA from fish bones via different methods like calcination, alkaline hydrothermal hydrolysis, and polymer assisted. The presence of some elements like sodium and magnesium has made this derived HA more effective and compatible than the synthetic one. In addition, the higher biocompatibility of HA obtained from fish bones is a result of higher Ca/P ratio as well as formation of B-type carbonated HA in this type of HA. Finally, the low price of raw materials attracts researchers to work on extraction of HA from these cheap resources [22, 23, 26–28].

Many researches have shown the adsorption characteristics of HA for purification of industrial waste waters and aqueous

solutions. HA particles are capable of adsorption of heavy metals like cadmium, lead, arsenic, aluminum, and nickel from the environment. In fact, the adsorption of these elements is done through replacing them with calcium ions presented in the structure of HA [29–31]; besides, HA is capable of acting as an anion, as well. It has been reported that sorption is accomplished by ionic exchange reaction with phosphate and hydroxyl groups to purify fluoride and chloride ions [32].

One of the heavy metals which seem to be toxic and common in industrial wastewater is nickel. Varieties of industries (same as electronic industries, automotive, zinc-based alloyed casting, and silver refineries) have polluted the environment with the large quantity of Ni^{2+} [33, 34]. There are a few researches which focused on the adsorption of nickel from aqueous solutions using HA as an adsorbent [35].

In the present study, Redmouth grouper (*Aethaloperca rogaa*) bones were used to isolate HA via the thermal calcination method. Different methods were used to characterize the obtained powders and also they were evaluated to compare the efficiency of them in nickel adsorption from aqueous solution. Langmuir and Freundlich isotherms were used to examine the capability of fish-derived HA for nickel adsorption from aqueous solutions.

2 Experimental Procedures

2.1 Materials and Methods

Fish scale was collected from a local store in Tehran, the capital city of Iran. The fish bones were boiled for 2 h to remove the adherent fish meat, salt, and organic impurities. After that, fish bones were dried at room temperature in the air for about 24 h. The dried bones were cut into smaller pieces and calcined in a furnace at 750 °C with a heating rate of 10 °C min⁻¹ followed by maintaining at this temperature for 6 h and then cooled to room temperature overnight. Finally, the calcined bones were milled using fast milled device and then passed through a 325-mesh sieve. Also, the commercial hydroxyapatite (CHA) supplied by Sigma-Aldrich, Fluka 21223, was used to compare fish bone-derived hydroxyapatite (FHA) with commercial HA in terms of morphology, chemical composition, biological characterization and Ni adsorption.

2.2 Characterization of FHA Powders

A Philips PW 1800 X-ray diffractometer (XRD) with irradiation source of Cu-K α was used to determine the phase composition of FHA. The data were collected over the 2θ range of 5° to 80° at a scan rate of 2° per minute. The peaks were normalized with respect to the most intense peak to obtain relative intensity and the resultant spectra were compared with

ICDD (JCPDS) standards to identify the phases. Fourier transform infrared spectroscopy (FT-IR) was used to investigate the compounds and functional groups using SHIMADZU (IRsolution) 8400S using potassium bromide (KBr) pellet technique. The spectra were obtained within the range of 360 to 4600 cm^{-1} . The Ca/P ratio and also the other elements including heavy metals were acquired by inductively coupled plasma-optical emission spectroscopy (ICP-OES). The analysis was performed using Optima 8000 by digesting 0.25 g of FHA into 50 ml acidic solution containing 0.1 M HCl. The emitted lines at 317.933 and 213.617 were used to calculate the contents of Ca and P, respectively. The experiment was repeated three times and the mean values are reported as the results. In order to compare the morphology and local chemical composition of FHA and CHA, a scanning electron microscopy (SEM, TESCAN/VEGA) equipped with energy-dispersive spectroscopy (EDS) was used. The powders were coated with gold before taking images at an accelerating voltage of 30 kV.

2.3 In Vitro Cell Culture

Evaluating and comparing the biological response of FHA and CHA were acquired using the MG-63 cells, human osteosarcoma (NCBI C-555; National Cell Bank of Iran, Pasteur Institute of Iran, Tehran, Iran), cultured in Dulbecco's modified Eagle medium (DMEM) (GIBCO, Scotland) with 10% (v/v) fetal bovine serum (FBS-Serumed, Germany), 100 U ml^{-1} penicillin, 100 $\mu\text{g ml}^{-1}$ streptomycin (Sigma, USA), and incubated at 37 °C in a humidified atmosphere containing 5% CO_2 .

2.3.1 Extraction

The samples of FHA and CHA were used to calculate the rates of proliferation and differentiation. The sterilization of powders was done using autoclave process at 120 °C under the pressure of 1.5 kg cm^{-2} for 1 h. The obtained samples were prepared by soaking them into DMEM at different concentrations of FHA and CHA (5, 10, 20, 50, and 100 $\mu\text{g ml}^{-1}$), then incubated for 24 h. The media were gathered for use in different cellular assays and pure culture medium held under similar conditions to use as negative control.

2.3.2 Cell Proliferation Assay

The toxicities of FHA and CHA were analyzed by conducting MTT assay which is based on the rule that a live cell change yellowish MTT into an insoluble purple formazan crystal. 3×10^3 cells well^{-1} plus 100 μl culture mediums were cultured into 96 well culture plates (Nunc, Denmark). The culture medium was rinsed and replaced by 90 μl of extract samples with 10 μl of FBS 24 h later. After 1 day, the medium was removed

and 100 μl of MTT solution (0.5 mg ml^{-1} (Sigma, USA)) was added. Then, another time, the cells had been incubated at 37 °C for a period of 4 h. Afterward, 100 μl of isopropanol (Sigma, USA) was added to each well to solubilize the formazan crystals. Eventually, the optical density of formazan was measured at 545 nm using multiwell microplate reader (STAT FAX 2100, USA). This experiment was repeated three times and the results were normalized with respect to the control sample.

2.3.3 Cell Differentiation

In order to evaluate the effects of FHA and CHA on the differentiation of MG-63 osteoblast cells, the extracted samples at different concentrations of FHA and CHA (5, 10, 20, 50, and 100 $\mu\text{g ml}^{-1}$) were placed into each well of the 96-well plates. One day later, 3000 cells in the volume of 50 μl culture media were added to each well and were located in the incubator for 4–5 h. After adhesion of cells, a specific amount of culture medium was added to each well. After every 5 days, a specific amount of fresh culture medium was added into each well until day 10. After 10 days, the medium was removed and alkaline phosphatase (ALP) activity was analyzed by Auto-Analyzer (Hitachi 902, Germany, Pars Azmoon kit, Iran) device. This experiment was repeated three times and the results were normalized with respect to the control sample.

2.4 Adsorption of Ni^{2+}

Batch equilibrium technique was performed to evaluate the adsorption characteristics of FHA for Ni^{2+} and compare the adsorption properties of FHA with CHA. The Ni^{2+} adsorption versus contact time, the initial concentration of Ni^{2+} , and the dosage of adsorbent was measured to determine the optimum condition of Ni^{2+} from aqueous solution.

The initial solutions of Ni^{2+} were prepared by dissolving predetermined amount of nickel sulfate ($\text{NiSO}_4 \cdot 7\text{H}_2\text{O}$, Sigma-Aldrich No. 227676) in distilled water. In the adsorption isotherm experiments, 0.4 g of FHA and CHA was added to a stirred tank reactor containing 500 ml of solutions. The initial concentrations of nickel were 30, 40, 60, and 80 mg l^{-1} and pH values were regulated to the value 6 by addition of HCl or NaOH. The solution was stirred at 300 rpm at 27 °C. At the end of predefined time intervals (5, 10, 20, 30, 60, 120, and 300 min), the solutions were filtered by filter paper (Whatman grade 6) and the precise concentration of residual Ni^{2+} was measured using atomic absorption spectrophotometer (AA990F pg instruments).

The adsorption percentage and the adsorption capacity (q_e , mg g^{-1}) were obtained using the following equations:

$$\% \text{ adsorption} = ((C_0 - C_e)/C_0) \times 100 \quad (1)$$

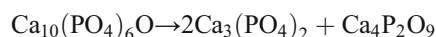
$$q_e = (C_0 - C_e) \times V/W \quad (2)$$

Where C_0 (mg l^{-1}) is the initial Ni concentration in the solution, C_e (mg l^{-1}) is the concentration of Ni at the equilibrium state, and V (l) and W (g) are the volume of solution and the mass of adsorbent, respectively.

3 Results and Discussion

3.1 Characterization of Obtained Powder

The XRD pattern of obtained powder from fish bone can be seen in Fig. 1a. Also, the resulting XRD pattern was compared with standard HA JCPDS (9-432) card. As we can see, the majority of FHA peaks are fitted with those of standard spectra which confirmed the HA composition. A very weak peak at $2\theta = 34.7$ seems to be related to β -TCP as we compared the spectra with standard β -TCP JCPDS card (86-1585). However, in the standard spectra, this band possesses the highest relative intensity diffracting from (-110) indicating that the amount of β -TCP is negligible. The previous study [8] showed that as the calcination temperature increased from 600 to 900 $^{\circ}\text{C}$, phase composition changed from pure HA to mixture of HA- β -TCP. A similar result was obtained by another study which demonstrated that the concentrations of β -TCP in the mixture were up to 30%wt [27]. As stated by Liao et al. [36], the heating of HA resulted in release of OH^- and finally transformation of hydroxyapatite to oxyapatite ($\text{Ca}_{10}(\text{PO}_4)_6\text{O}$, OAP) and then to different calcium phosphate materials (i.e., tricalcium phosphate and tetracalcium phosphate) due to lattice destruction according to the reaction:



The (002), (211), (300), and (310) diffractions were used to calculate the mean crystallite size of particles, t , by means of Scherrer's equation [37]:

$$t = \frac{k\lambda}{\beta \cos \theta} \quad (3)$$

where k refers to a dimensionless shape factor, the Scherrer constant (generally assumed to be 0.9), λ is the wavelength of X-ray radiation, β is the line broadening at half the maximum intensity in radians, and θ is the Bragg angle. The calculated mean crystallite size of particles is about 40 nm.

The infrared absorption spectra of the obtained powder (FHA) are plotted in Fig. 1b. The FT-IR spectra explain the chemical structure of the FHA. The characteristic bands of PO_4^{3-} appeared in two main regions. The first one represented by the 1045 and 1093 cm^{-1} peaks indicates ν_3 stretching asymmetric stretching mode. The second one demonstrated

by the 569 and 603 cm^{-1} peaks corresponds to ν_4 bending mode. The typical band of carbonate is detected at 871 cm^{-1} . In addition, the bands between 1500 and 1417 were produced from asymmetric stretch mode (ν_3) of CO_3^{2-} . The hydroxyl group (OH^-) was recognized by the peak at 3570 cm^{-1} , corresponding to stretching mode of hydroxyl group, and 633 cm^{-1} , corresponding to liberation mode of hydroxyl group.

Table 1 demonstrates the elemental analysis as well as Ca/P molar ratio of FHA. The results showed that calcium and phosphorus are the major components of the FHA. In addition, the concentrations of other elements like sodium, magnesium, strontium, and potassium were reported. Furthermore, the concentrations of other elements including heavy metals were less than 10 ppm which is negligible. The resulting Ca/P was 1.72 which is slightly higher than 1.67 observed in human bones. This higher Ca/P ratio could be the result of substitution of phosphate group by carbonate ions and formation of B-type carbonate HA. However, the possibility of substitution of calcium with other cations like Mg^{2+} and formation of magnesium apatite, $\text{Ca}_{10-x}\text{Mg}_x(\text{PO}_4)_6(\text{OH})_2$, could be another reason for this slight increase.

Figure 2 displays the resulting SEM and EDS analyses of FHA and CHA. As we can see in Fig. 2a, the FHA powder has an irregular spherical shape and the particles are in the micro-scale order. As shown in Fig. 2a and b, the FHA and CHA particles have no considerable difference in terms of morphology and particle size. The EDS spectroscopy of FHA (Fig. 2c) revealed that the FHA powder consists of oxygen, phosphorus, calcium, magnesium, and sodium atoms. Calcium and phosphorus in the form of carbonate and phosphate are the main components of FHA. In contrast, the EDS result of CHA revealed that the powders consist of the typical elements found in pure HA and no other element was observed in the spectra (Fig. 2d). Also, these results illustrate that the relative Ca/P ratio in FHA is 1.75 which is higher than the theoretical value (1.67). In addition, the resulting Ca/P from EDS was in accordance with those of ICP-OES.

In order to evaluate the cytotoxicity of the obtained powder and compare with CHA powder, they were co-cultured with MG-63 cells. Figure 3a demonstrates the cytotoxicity characteristics of FHA and CHA at various concentrations. As we can see, no evidence of toxicity among the extracts of the test materials up to concentration of 20 $\mu\text{g ml}^{-1}$ was observed and all of the samples below this range were in-toxic. Viability of FHA had an upward trend from the concentrations of 5 to 10 $\mu\text{g ml}^{-1}$. The rate of viability decreased at the concentrations exceeding 20. Briefly, in comparison with CHA, FHA presented an almost similar rate of MG-63 cell viability.

The effect of the FHA on the osteoblastic phenotype was evaluated and compared through ALP production by MG-63 cells. Typically, the ALP production increases in parallel with

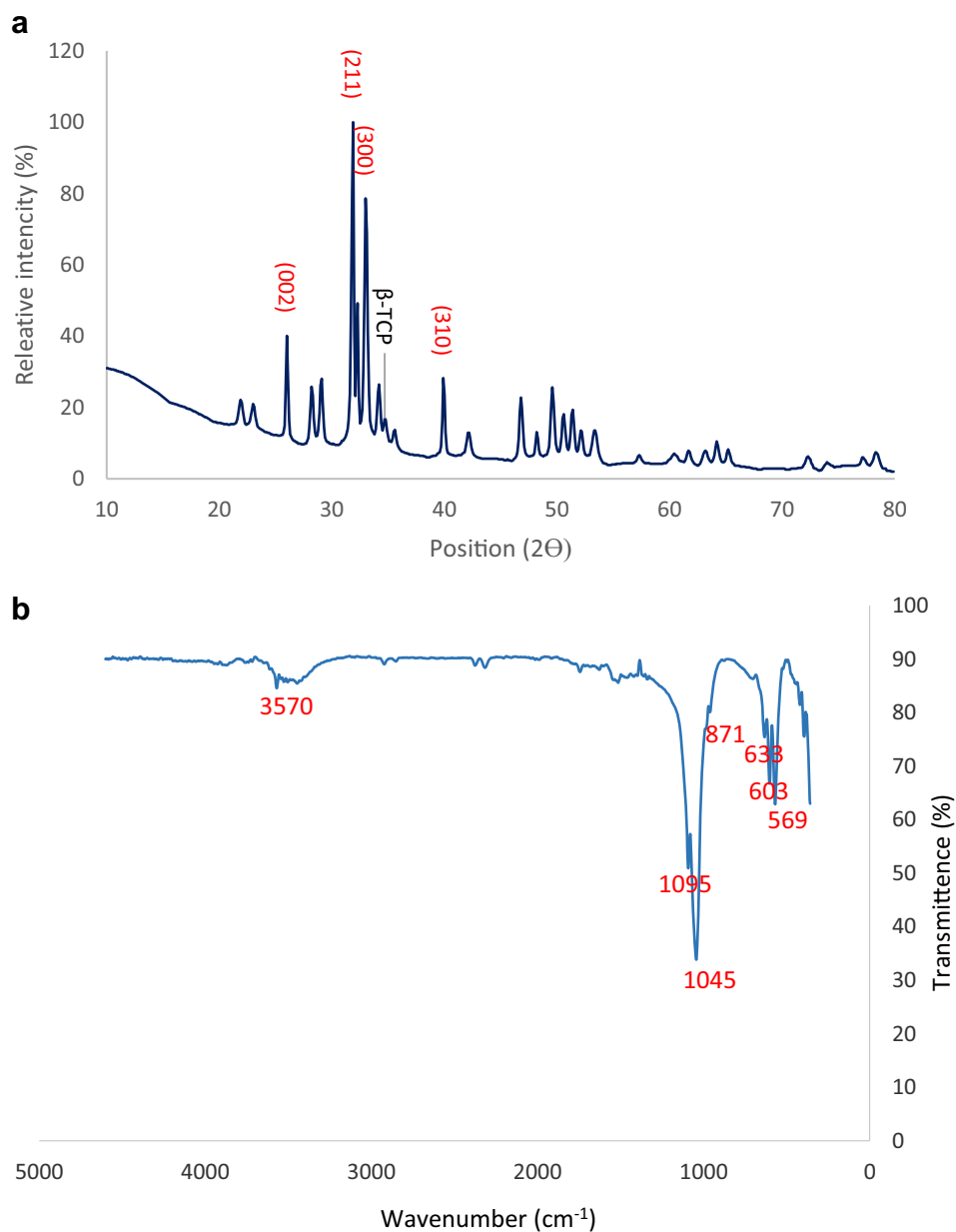


Fig. 1 **a** XRD and **b** FT-IR spectra of FHA

the number of osteoblast cells. Figure 3b shows the resulting ALP production after 10 days. ALP production over the FHA at different concentrations was seen to peak at the concentration of $10 \mu\text{g ml}^{-1}$. The ALP production by FHA and CHA did not change significantly except for the highest dosage of CHA. In addition, in comparison with CHA, the amounts of ALP production at different concentrations of FHA by the

cells were almost similar and were in the desirable level. The results imply that the MG-63 cells were effectively affected by FHA powders on promoting cell differentiation.

3.2 Adsorption of Nickel

Adsorption of heavy metals by HA depends on the surface area and crystallinity of HA powders so that higher surface area and less crystallinity will yield to higher adsorption capacity [38]. Besides, among all the heavy metals, Pb is highly adsorbed by HA since it is borderline hard Lewis acid and has high electronegativity [29]. Also, cations with radii higher than that of Ca^{2+} (0.099 nm) have better chance to adsorb by

Table 1 Elemental analysis characterized by ICP-OES (% w w⁻¹)

Sample	Ca	K	Mg	Na	Sr	P	Ca/P molar ratio
FHA	42.75	0.12	0.62	0.78	0.14	19.2	$1.72 \pm .02$

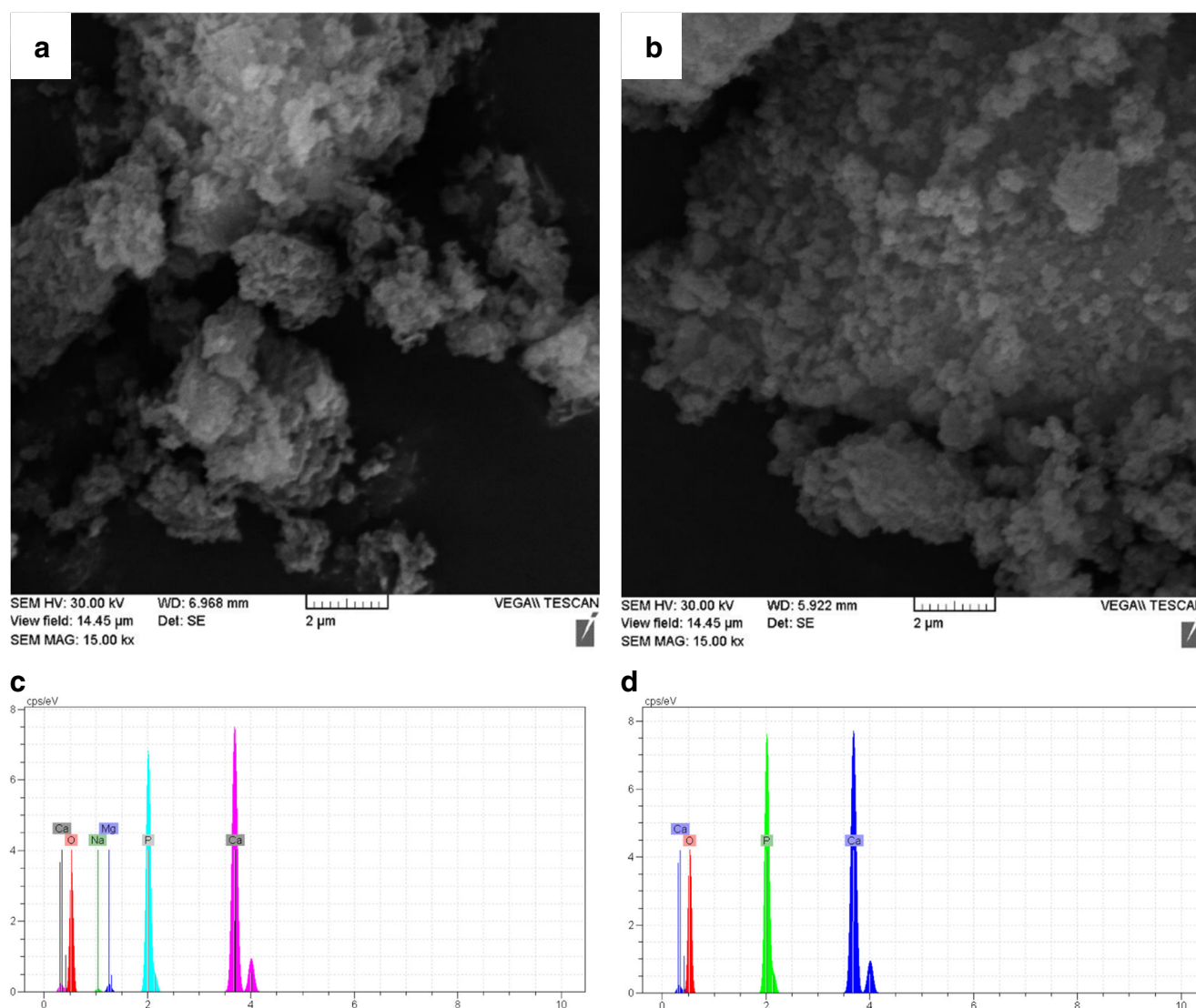
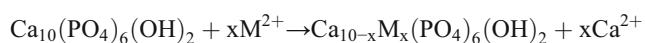


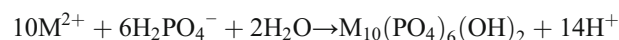
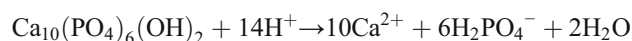
Fig. 2 SEM micrographs for **a** FHA, and **b** CHA and EDS spectra for **c** FHA and **d** CHA powders

HA compared to cations with smaller radii, as stated by LeGerose et al. [39]. For instance, a lower amount of Ni^{2+} is adsorbed by HA in comparison with Cd^{2+} (0.097 nm) and Pb (0.118 nm) [29, 31].

As mentioned before, there have been numerous works which confirmed the capability of HA to adsorb metal ions through two main mechanisms. The first one is ion exchange in which calcium ions in the HA lattice are replaced by the adsorbed metal ions through diffusion process [40].



The other mechanism seems to be precipitation of metal-phosphate compound materials in acidic conditions. In this condition, phosphate reacts with metallic ions according to the following equation and forms a new crystalline structure which has low solubility [40].



Mobasherpour et al. [35] have reported that the adsorption was carried out through two-step adsorption procedure. Initially, the nickel ions adsorbed rapidly via surface complexation with $=\text{POH}$ sites and then formation of $\text{Ca}_{10-x}\text{M}_x(\text{PO}_4)_6(\text{OH})_2$. In other words, the first step is adsorption of nickel by HA which is followed by substitution of Ca^{2+} by Ni^{2+} .

3.2.1 Effect of Initial Concentration of Ni^{2+}

The effect of initial concentration of nickel seems to be a significant matter to dominate all the mass transfer limitations of nickel between the aqueous and solid phases. Different concentrations of Ni^{2+} (30, 40, 60, and 80 mg l^{-1}) were chosen to evaluate the adsorption of nickel by FHA and CHA from

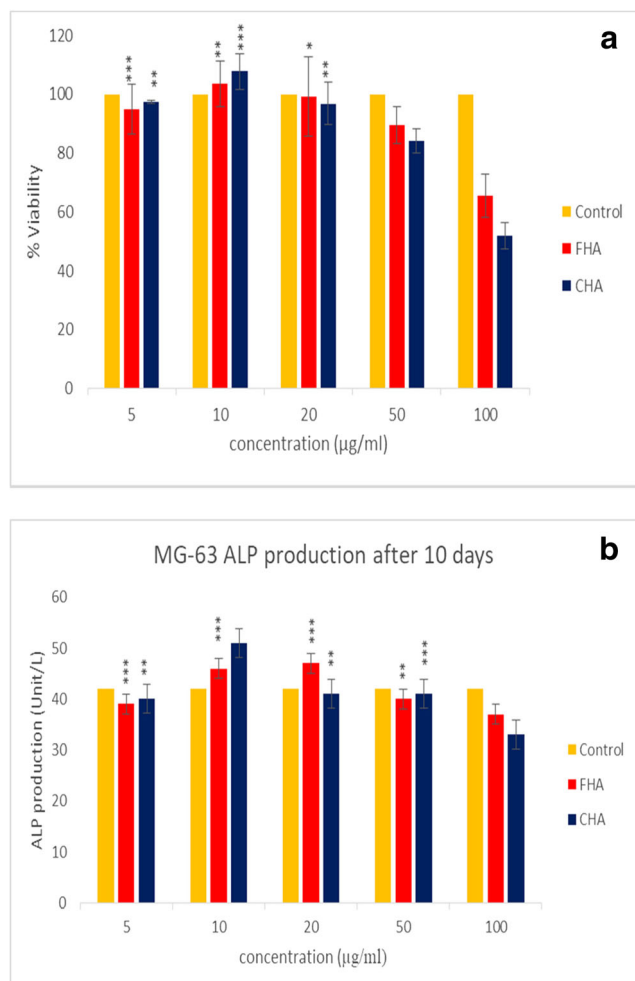


Fig. 3 Effect of different concentrations of FHA and CHA powders on **a** viability of MG-63 after 24 h and **b** alkaline phosphatase production of MG-63 cells after 10 days

aqueous solutions. The following conditions were applied to the solutions: pH = 6; HA dosage 0.8 g l^{-1} ; temperature 27°C ; rotation speed 300 rpm; and time 24 h. The effect of various initial concentrations of nickel on nickel adsorption is shown in Fig. 4a. The equilibrium adsorption capacity was plotted as a function of initial concentration. It can be seen that the adsorption capacity enhanced in parallel with the increase in the initial concentration of nickel. It can be concluded that a higher initial concentration of nickel would result in superior adsorption capacity. The maximum adsorption capacity at the initial concentration of 80 mg l^{-1} for FHA and CHA is 40.92 and 38.86 mg g^{-1} , respectively. As we can see, there is no significant difference in adsorption capacity of FHA and CHA, indicating that FHA powder seems to be an appropriate sorbent to remove nickel from aqueous solutions.

3.2.2 Effect of Adsorbent Dosage

Figure 4b demonstrates plot of adsorption of nickel versus different adsorbent dosages. On one hand, adsorption

percentage of both adsorbent increased with increasing adsorbent mass. About a 10% growth in adsorption percentage was quite noticeable with the increase of the FHA and CHA dosages in the range of 0.8 to 1.4 g. Increasing the dosage of the adsorbents resulted in higher active sites as well as higher surface area leading to increase of the removal of Ni^{2+} ions [35]. The optimum amount of adsorbent was 1.2 g and after that the adsorption percentage was almost equal to that of 1.2 g. On the other hand, as the adsorbent dosage increased, the adsorption capacity reduced and it was seen that the adsorption capacity was low at high dosages of FHA and CHA. The unsaturated nature of the adsorbent played the major role in the adsorption capacity reduction. In addition, the adsorption performance of FHA was quite comparable with that of CHA and at a lower dosage of adsorbent, FHA performance was better than that of CHA.

3.2.3 Effect of Contact Time

Figure 4c illustrates the adsorption capacity of FHA and CHA as a function of contact time at 80 mg l^{-1} of the initial concentration of nickel. As we can see in Fig. 4c, the rate of adsorption capacity had a sharp upward trend at the primary part of contact time. This was followed by a slow increase in the adsorption capacity until the equilibrium was reached. It was found that the equilibrium time for either adsorbent at the dosage of 0.8 g l^{-1} and rotation speed of 300 rpm seems to be 120 min. However, what we should bear in mind is that the necessary contact time to reach the equilibrium is 24 h and beyond that the effects of contact time are negligible. Therefore, we can divide the adsorption process into two periods: the first one includes rapid adsorption of nickel ions on the outer surface of adsorbents; once the exterior surface of adsorbent fully saturated, the second period of adsorption would start. In the second period, the adsorption is performed via diffusing of nickel ions into the inner surface of the adsorbent [41].

3.3 Adsorption Kinetic of Nickel

The first-order kinetic model, pseudo-second-order kinetic model, and intraparticle diffusion kinetic model have been employed to determine the controlling adsorption mechanism like mass transfer and chemical reaction. The simplest analysis of adsorption kinetics is the first-order kinetic model which is extensively used to describe the adsorption of solute from aqueous solutions [42]. The following equation shows the first-order kinetic model:

$$1/q_t = (k_1/q_1) (1/t) + 1/q_1 \quad (4)$$

where q_t is the amount of nickel adsorbed at different times and also q_1 is the equilibrium adsorption of nickel on the

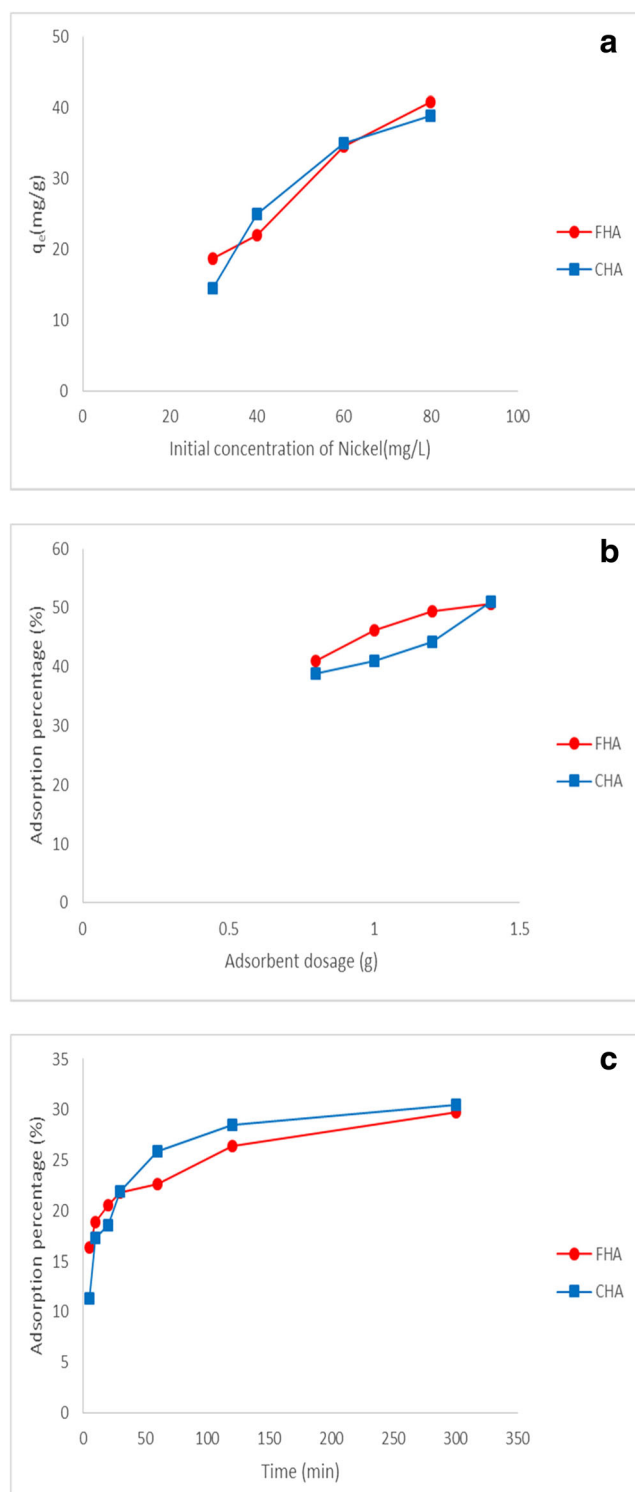


Fig. 4 Nickel adsorption with respect to changes in **a** initial concentration of nickel, **b** adsorbent dosages, and **c** contact time. General parameters are adsorbent dosage 0.8 g l^{-1} , initial nickel concentration 80 mg l^{-1} , pH = 6, contact time 24 h, and rotation speed 300 rpm

adsorbent (mg g^{-1}); k_1 expresses the rate constant of the first-order kinetic model (min^{-1}). The first-order constants can be characterized from the intercept and slope of the plot obtained by drawing $1/q_t$ versus $1/t$ (Fig. 5a).

Equation 5 shows the linear form of pseudo-second-order kinetic model [43]:

$$t/q_t = (1/(k_2 q_2^2)) + t/q_2 \quad (5)$$

where q_t and q_2 are the adsorbed quantity at the instant t and maximum adsorption capacity (mg g^{-1}), respectively; k_2 is the rate constant of pseudo-second-order kinetic model (g (mg min)^{-1}). The slope and intercept of the plot of t/q_t versus t (Fig. 5b) is used to calculate the value of k_2 and q_2 .

The previous models are not capable of specifying the diffusion mechanism. Hence, another simple adsorption kinetic model, intraparticle diffusion model, had been used to characterize the diffusion mechanism [43]. The rate of intraparticle diffusion can be calculated based on the following equation:

$$q_t = k_i t^{0.5} + C \quad (6)$$

where q_t (mg g^{-1}) is the amount of nickel adsorbed at time t , k_i ($\text{mg (g min}^{0.5})^{-1}$) is the intraparticle diffusion rate constant, and C is the intercept which is proportional to the boundary layer thickness (mg g^{-1}). The values of k_i and C are the slope and intercepts of the plot of q_t versus $t^{0.5}$ (as shown in Fig. 5c).

Table 2 indicates the kinetic parameters for nickel adsorption at 27°C obtained from the three adsorption kinetic models. As we can see, the values of q_2 for FHA and CHA were 30.4 and 31.65, respectively, and the linear coefficient, R^2 , was up to 0.999. For both adsorbents, the theoretical values calculated from pseudo-second-order were almost in agreement with the experimental ones. Hence, this implies that the pseudo-second-order model is quite fitted for adsorption of nickel on FHA and CHA. In addition, the results indicate that FHA and CHA express similar characters in terms of adsorption kinetic and adsorption sites.

The intraparticle diffusion plot for nickel adsorption on FHA and CHA is illustrated in Fig. 5c. This model was used to determine the rate-controlling adsorption process. If the linear plot of the intraparticle diffusion passes through the origin, the rate-controlling step is intraparticle diffusion; otherwise, other mechanisms are involved [44]. As we can see, none of the intraparticle plot (Fig. 5c) has gone through the origin indicating that the intraparticle diffusion is not the only rate-controlling mechanism. The value of C , intercept of plot of q_t vs $t^{0.5}$, implies some degree of boundary layer control [44]. The value of C was higher for FHA in comparison with that of CHA which implies more surface adsorption of nickel on FHA. Thus, adsorption of nickel on FHA and CHA is controlled by both surface adsorption and intraparticle diffusion.

3.4 Adsorption Isotherm

The adsorption isotherms have been used to describe adsorption interaction between liquid phase and adsorbent and

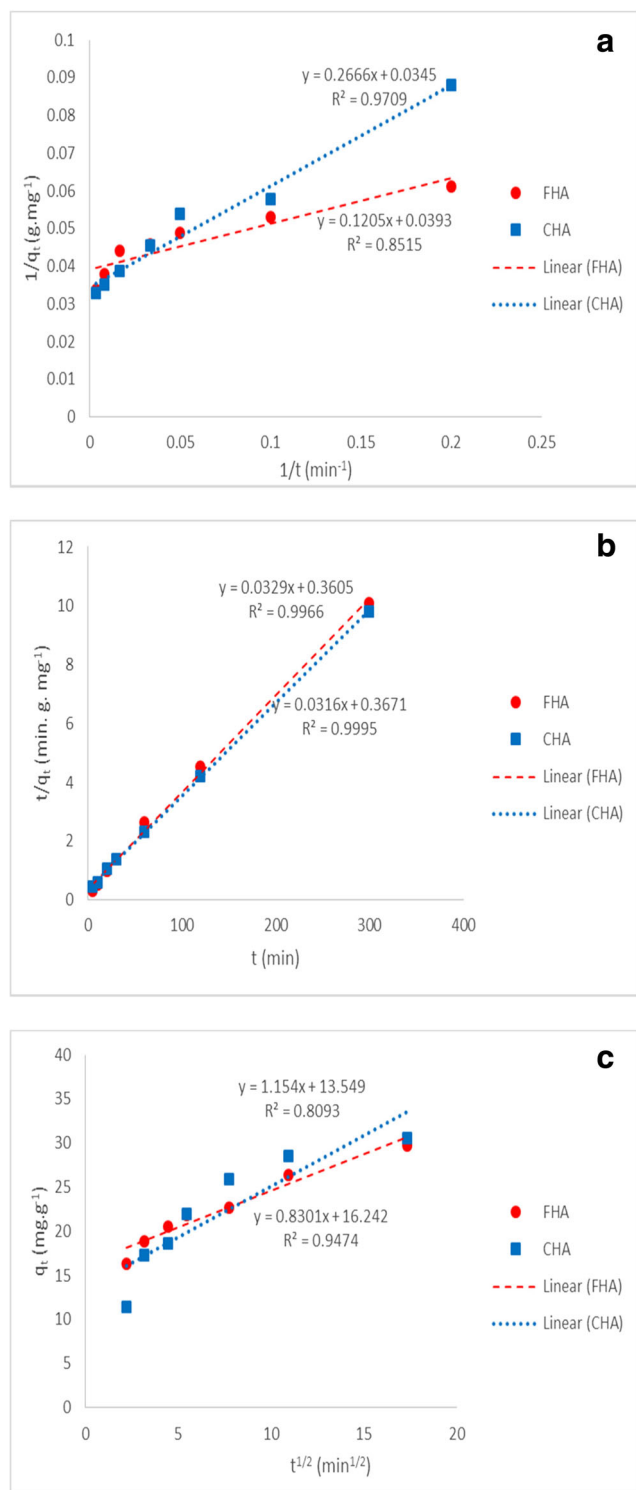


Fig. 5 The **a** first-order, **b** pseudo-second-order, and **c** intraparticle diffusion kinetic models of nickel adsorption on FHA and CHA at 27 °C

determine the adsorption mechanism for removing the heavy metals. The adsorption isotherms express the relationship between the amount of adsorbed nickel and the remaining nickel in the solution to predict the adsorption parameters and also adsorption behavior of the adsorbent. Besides, what we should

bear in mind is that the shape of isotherm can help us figure out about the adsorption procedure. Giles et al. had categorized the adsorption isotherm into four groups of L, S, H, and C [45]. As we can see in Fig. 4a and according to the abovementioned categorization, the adsorption of nickel on to adsorbent has fallen into L category which indicates lack of strong completion between the solvent and the adsorbate in occupation of adsorbent surface sites [46]. The Langmuir, Freundlich, and DKR (Dubinin-Kaganer-Radushkevich) models are the most widely employed models to explain adsorption behavior of different adsorbents.

The most prevalent used adsorption model to describe adsorption isotherm at a certain temperature is the Langmuir model. The Langmuir model assumes that the surface of adsorbing sites is energetically homogenous and each site is capable of accommodating at most one molecule to form a monolayer coverage. In addition, the model assumes that the adsorption takes place only at particular sites without any interaction between the adsorbent molecules [47]. The linear mathematical equation of the Langmuir equation is represented by the following equation:

$$C_e/q_e = C_e/q_m + 1/q_m K_L \quad (7)$$

where C_e (mg l⁻¹) is the concentration of nickel at equilibrium; q_e is the amount of nickel adsorbed per unit weight of adsorbent at equilibrium (mg g⁻¹); q_m is the maximum amount of nickel adsorbed per weight unit of the adsorbent (mg g⁻¹); K_L is Langmuir constant related to sorption energy. The values of q_m and K_L can be calculated from the slope and intercept of linear plot of C_e/q_e versus C_e (Fig. 6a).

Freundlich model is an empirical adsorption model which describes the adsorption capacity as a function of equilibrium nickel concentration. This model is mainly used to describe surface heterogeneity and also distribution of active site and their energy [48]. The linear form of Freundlich isotherm equation is given by the following equation:

$$\ln q_e = \ln k_F + \frac{1}{n} \ln C_e \quad (8)$$

where q_e is the amount of nickel adsorbed per gram of adsorbent; C_e is equilibrium nickel concentration; n and k_F [(mg g⁻¹) (l mg⁻¹)^{1/n}] are Freundlich constants which can be calculated by plotting $\ln(q_e)$ versus $\ln(C_e)$ (Fig. 6b).

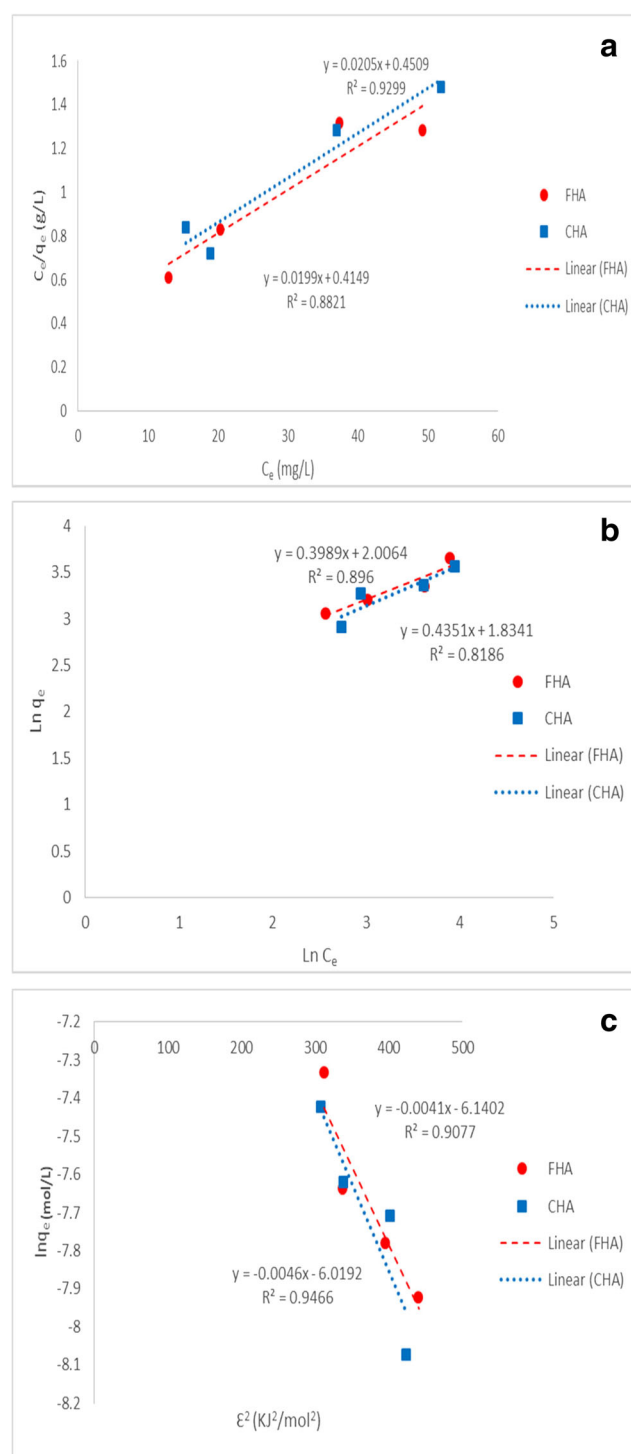
Since the previous models are not capable of explaining the physical and chemical properties of adsorption, the Dubinin-Kaganer-Radushkevich (DKR) isotherm model is used to characterize the adsorption isotherm of a single-solute system [49]. The linear form of DKR equation is expressed as:

$$\ln q_e = \ln X_m - \beta \epsilon^2 \quad (9)$$

where X_m (mol g⁻¹) is related to the degree of sorbate adsorption by the sorbent, β (mol² J⁻²) is Dubinin-Kaganer-

Table 2 Adsorption kinetic parameters and adsorption isotherm constant for nickel adsorption by FHA and CHA at 27 °C

Adsorption kinetic									
Adsorbent	q_{e-exp} (mg g ⁻¹)	First order		Pseudo-second-order		Intraparticle diffusion		R^2	C (mg g ⁻¹)
		q_1 (mg g ⁻¹)	k_1 (min ⁻¹)	q_2 (mg g ⁻¹)	k_2 [g (mg min ⁻¹) ⁻¹]	K_i [mg (g min ^{1/2}) ⁻¹]	X_m (mol g ⁻¹)		
FHA	29.71	22.45	3.07	30.40	0.0030	0.83		0.996	16.24
CHA	30.53	28.99	7.73	31.65	.0027	1.154		0.999	13.55
Adsorption Isotherm	Adsorbent	Langmuir isotherm		Freundlich isotherm		DKR isotherm		R^2	β (mol ² J ⁻¹)
		q_1 (mg g ⁻¹)	K_L (l mg ⁻¹)	K_F [(mg g ⁻¹) (l mg ⁻¹) ^{1/n}]	N	X_m (mol g ⁻¹)			
FHA		50.25	0.048	7.436	2.006	114.43		0.896	-4×10^{-5}
CHA		48.78	0.045	6.259	2.299	101.49		0.819	-5×10^{-5}

**Fig. 6** The **a** Langmuir, **b** Freundlich, and **c** DKR adsorption isotherm plots for nickel adsorption onto FHA and CHA at 27 °C

Radushkevich constant related to the mean sorption energy, and ε is called the Polanyi potential which is given by the following formula:

$$\varepsilon = RT \ln(1 + 1/C_e) \quad (10)$$

Table 3 Comparison of maximum adsorption capacity of Ni²⁺ onto different adsorbents

Item	Adsorbent	q_m (mg g ⁻¹)	Reference
1	Na-bentonit	13.96	51
2	γ-Alumina nanoparticles	34.14	52
3	Treated polyurethane foam	24.39	53
4	Modified coir pith	38.9	54
4	Chitosan	76	55
5	Porous graphene oxide/sawdust	131.93	56
6	Clinoptilolite	5.08	57
7	Vermiculite	15.76	58
8	Zeolite	5.52	58
9	Bentonite	8.93	58
10	Activated carbon–zeolite composite	70.43	59
11	Macroporous chitosan	10.3	60
12	Activated sludge	238.10	61
13	Synthesized nanocrystalline HA	46.17	35
14	Fish bone-derived HA	50.25	Present study
15	Commercial HA	48.78	Present study

where R is the gas constant (J mol K⁻¹) and T is temperature (K). The values of β and X_m can be obtained from the slope and intercept of the linear plot of $\ln q_e$ versus ε^2 (Fig. 6c). Besides, what we should consider is that the constant β gives sorption energy (E) which is useful to have some information about physical and chemical features of adsorption (Eq. 11).

$$E = (-2\beta)^{-0.5} \quad (11)$$

The amounts of sorption energy help us identify the dominant adsorption type. If the E value was less than 8 kJ mol⁻¹, the adsorption type would be characterized by physical type of adsorption, if the E value is into the range of 8–16 kJ mol⁻¹ the ion exchange would govern the adsorption, and for the values higher than 16 kJ mol⁻¹ the chemical adsorption, stronger than ion exchange, would explain the adsorption type [50]. In addition, the calculated sorption energies for FHA and CHA, according to DKR model, were 11.04 and 10.43 kJ mol⁻¹, respectively. The results indicate that the experimental datum properly fitted DKR for adsorption of Ni on FHA and CHA.

Table 2 illustrates the Langmuir, Freundlich, and DKR adsorption isotherm constants for both adsorbents. As we can see, the adsorption parameter fitted with DKR and Langmuir by comparing the correlation factor (R). The maximum values of adsorbed nickel per weight unit of FHA and CHA, q_m , were 50.25 and 48.78 mg g⁻¹, respectively.

In addition, Table 3 demonstrates the comparison between the maximum monolayer adsorption capacities of nickel onto a variety of adsorbents. It shows that FHA used in this study seems to have a proper capability to adsorb nickel from aqueous solutions.

4 Conclusion

The FHA was extracted from the fish scales via the calcination method. This powder was characterized using a variety of methods such as XRD, FT-IR, ICP, MTT, ALP assay, and SEM. The MTT result indicated that the FHA expressed proper cell viability and it has a higher Ca/P ratio than stoichiometric ratio as shown by elemental analysis. In addition, the FHA showed almost similar adsorption capacity and kinetic to CHA. The adsorption kinetics was consistent well with the pseudo-second order and the adsorption isotherm followed the Dubinin-Kaganer-Radushkevich model. Therefore, the present study resulted in extraction of HA from fish scales which are cheap and useful and according to the preliminary biological assays, it seems to have a good potential for further investigation on its bioapplications. Besides, the adsorption behavior of FHA is quite comparable with that of CHA. Further investigations are being carried out in our lab.

References

1. F. Yearbook, Fishery and aquaculture Statistics, 2013.
2. Elvevoll, E. O., & James, D. (2001). *Nutrition and Health*, 15, 155–167.
3. Ferraro, V., Cruz, I. B., Jorge, R. F., Malcata, F. X., Pintado, M. E., & Castro, P. M. (2010). *Food Research International*, 43, 2221–2233.
4. Gumisiriza, R., Mshandete, A. M., Rubindamayugi, F., Kansiime, F., & Kivaisi, A. K. (2009). *African Journal of Environmental Science and Technology*, 3, 013–020.
5. Pati, F., Adhikari, B., & Dhara, S. (2010). *Bioresource Technology*, 101, 3737–3742.
6. H.-J. Chai, J.-H. Li, H.-N. Huang, T.-L. Li, Y.-L. Chan, C.-Y. Shiau, C.-J. Wu, *Journal of BioMed Research*, 2010 (2010).
7. Chen, S., Hirota, N., Okuda, M., Takeguchi, M., Kobayashi, H., Hanagata, N., & Ikoma, T. (2011). *Acta Biomaterialia*, 7, 644–652.
8. Boutinguiza, M., Lusquiños, F., Comesaña, R., Riveiro, A., Quintero, F., & Pou, J. (2007). *Applied Surface Science*, 254, 1264–1267.
9. Boutinguiza, M., Lusquiños, F., Riveiro, A., Comesaña, R., & Pou, J. (2009). *Applied Surface Science*, 255, 5382–5385.
10. Suchanek, W., & Yoshimura, M. (1998). *Journal of Materials Research*, 13, 94–117.
11. H. Aoki, *Science and medical applications of hydroxyapatite*, Ishiyaku Euroamerica, 1991.
12. Hench, L. L. (1991). *Journal of the American Ceramic Society*, 74, 1487–1510.
13. Best, S., Porter, A., Thian, E., & Huang, J. (2008). *Journal of the European Ceramic Society*, 28, 1319–1327.
14. Zhang, H.-b., Zhou, K.-c., Li, Z.-y., & Huang, S.-p. (2009). *Journal of Physics and Chemistry of Solids*, 70, 243–248.
15. Rhee, S.-H. (2002). *Biomaterials*, 23, 1147–1152.
16. Pang, Y., & Bao, X. (2003). *Journal of the European Ceramic Society*, 23, 1697–1704.
17. Xu, J., Khor, K. A., Dong, Z., Gu, Y., Kumar, R., & Cheang, P. (2004). *Materials Science and Engineering: A*, 374, 101–108.
18. Tseng, Y.-H., Kuo, C.-S., Li, Y.-Y., & Huang, C.-P. (2009). *Materials Science and Engineering: C*, 29, 819–822.

19. Herliansyah, M., Hamdi, M., Ide-Ektessabi, A., Wildan, M., & Toque, J. (2009). *Materials Science and Engineering: C*, 29, 1674–1680.
20. Ooi, C., Hamdi, M., & Ramesh, S. (2007). *Ceramics International*, 33, 1171–1177.
21. Murugan, R., Ramakrishna, S., & Panduranga Rao, K. (2006). *Materials Letters*, 60, 2844–2847.
22. Huang, Y.-C., Hsiao, P.-C., & Chai, H.-J. (2011). *Ceramics International*, 37, 1825–1831.
23. Boutinguiza, M., Pou, J., Comesaña, R., Lusquiños, F., de Carlos, A., & León, B. (2012). *Materials Science and Engineering: C*, 32, 478–486.
24. Haberko, K., Bućko, M. M., Brzezińska-Miecznik, J., Haberko, M., Mozgawa, W., Panz, T., Pyda, A., & Zarebski, J. (2006). *Journal of the European Ceramic Society*, 26, 537–542.
25. Xiaoying, L., Yongbin, F., Duchun, G., Wei, C., & Eng, K. (2007). *Mater*, 342, 343.
26. Pallela, R., Venkatesan, J., & Kim, S. K. (2011). *Ceramics International*, 37, 3489–3497.
27. Piccirillo, C., Silva, M., Pullar, R., Braga da Cruz, I., Jorge, R., Pintado, M., & Castro, P. M. (2013). *Materials Science and Engineering: C*, 33, 103–110.
28. Kongsri, S., Janpradit, K., Buapa, K., Techawongstien, S., & Chanthai, S. (2013). *Chemical Engineering Journal*, 215, 522–532.
29. Mobasherpour, I., Salahi, E., & Pazouki, M. (2012). *Arabian Journal of Chemistry*, 5, 439–446.
30. Stötzel, C., Müller, F., Reinert, F., Niederdraenk, F., Barralet, J., & Gbureck, U. (2009). *Colloids and Surfaces B: Biointerfaces*, 74, 91–95.
31. Feng, Y., Gong, J.-L., Zeng, G.-M., Niu, Q.-Y., Zhang, H.-Y., Niu, C.-G., Deng, J.-H., & Yan, M. (2010). *Chemical Engineering Journal*, 162, 487–494.
32. Sugiyama, S., Matsumoto, H., Hayashi, H., & Moffat, J. B. (2000). *Colloids and Surfaces A: Physicochemical and Engineering Aspects*, 169, 17–26.
33. O'Connell, D. W., Birkinshaw, C., & O'Dwyer, T. F. (2008). *Bioresource Technology*, 99, 6709–6724.
34. Öztürk, A., Artan, T., & Ayar, A. (2004). *Colloids and Surfaces B: Biointerfaces*, 34, 105–111.
35. Mobasherpour, I., Salahi, E., & Pazouki, M. (2011). *Journal of Saudi Chemical Society*, 15, 105–112.
36. Liao, C.-J., Lin, F.-H., Chen, K.-S., & Sun, J.-S. (1999). *Biomaterials*, (19), 1807–1813.
37. C. Suryanarayana, M.G. Norton, X-ray diffraction: a practical approach, Springer, 1998.
38. Smiciklas, I., Onjia, A., Raicevic, S., Janackovic, D., Mitric, M., & Hazard, J. (2008). *Mater*, 152, 876.
39. LeGeros RZ, Legeros JP, Phosphate minerals, 45(1984) 351–385.
40. Stötzel, C., Müller, F. A., Reinert, F., Niederdraenk, F., Barralet, J. E., & Gbureck, U. (2009). *Colloids and Surfaces B: Biointerfaces*, 74, 91–95.
41. Gupta, N., Kushwaha, A. K., & Chattopadhyaya, M. (2012). *Journal of the Taiwan Institute of Chemical Engineers*, 43, 604–613.
42. Ho, Y., & McKay, G. (1998). *Process Safety and Environmental Protection*, 76, 332–340.
43. Lin, K., Pan, J., Chen, Y., Cheng, R., & Xu, X. (2009). *Journal of Hazardous Materials*, 161, 231–240.
44. Özcan, A. S., & Özcan, A. (2004). *Journal of Colloid and Interface Science*, 276, 39–46.
45. Giles, C. H., MacEwan, T. H., & Nakhwa, S. N. (1960). *Smith D. Journal of the Chemical Society*, 3973–3993.
46. Foroughi-dahr, M., Abolghasemi, H., Esmaili, M., Nazari, G., & Rasem, B. (2015). *Process Safety and Environmental Protection*, 95(226–236).
47. Ketcha Mbadcam, J., & Anagho, S. (2011). *Journal of Environmental Chemistry and Ecotoxicology*, 3, 290–297.
48. Augustine, A., Orike, B., & Edidiong, A. (2007). *EJEAFChe*, 6, 2221–2234.
49. Ketcha Mbadcam, J., Dongmo, S., & Dinka'a Ndaghu, D. (2012). *International Journal of Current Research*, 4, 162–167.
50. Wang, C.-C., Juang, L.-C., Lee, C.-K., Hsu, T.-C., Lee, J.-F., & Chao, H.-P. (2004). *Journal of Colloid and Interface Science*, 280, 27–35.
51. Liu, Z. R., & Zhou, S. Q. (2010). *Process Safety and Environmental Protection*, 88, 62–66.
52. Fouladgar, M., Beheshti, M., & Sabzyan, H. (2015). Equilibrium and kinetic modeling. *Journal of Molecular Liquids*, 30, 1060–1073.
53. Mangaleswaran, L., Thirulogachandar, A., Rajasekar, V., Muthukumaran, C., & Rasappan, K. (2015). *Journal of the Taiwan Institute of Chemical Engineers*, 55(112–118).
54. Ewecharoen, A., Thiravetyan, P., & Nakbanpote, W. (2008). *Chemical Engineering Journal*, 137, 181–188.
55. Kyzas, G. Z., & Kostoglou, M. (2015). *Separation and Purification Technology*, 149(92–102).
56. Wu, Y., Luo, H., Wang, H., Zhang, L., Liu, P., & Feng, L. (2014). *Journal of Colloid and Interface Science*, 436, 90–98.
57. Oter, O., & Akcay, H. (2007). *Water Environment Research*, 1, 329–335.
58. Katsou, E., Malamis, S., Haralambous, K. J., & Loizidou, M. (2010). *Journal of Membrane Science*, 360, 234–249.
59. Jha, V. K., Matsuda, M., & Miyake, M. (2008). *Journal of Hazardous Materials*, 160, 148–153.
60. Ghaee, A., Shariaty-Niassar, M., Barzin, J., & Zarghan, A. (2012). *Applied Surface Science*, 258, 7732–7743.
61. Aksu, Z., Açikel, Ü., Kabasakal, E., & Tezer, S. (2002). *Water Research*, 36, 3063–3073.